J Appl Electrochem (2012) 42:1065–1070
DOI 10.1007/s10800-012-0488-z

ORIGINAL PAPER

# A nanocomposite of graphene/$MnO_2$ nanoplatelets for high-capacity lithium storage

**Xinlu Li · Hongfang Song · Hao Wang · Yonglai Zhang · Kun Du · Hongyi Li · Jiamu Huang**

Received: 13 July 2012 / Accepted: 1 October 2012 / Published online: 11 October 2012


**Abstract** A nanocomposite of graphene/$MnO_2$ nanoplatelets was prepared by one-step chemistry route at room temperature. The microstructure was characterized by X-ray diffraction, $N_2$ absorption, scanning electron microscopy (SEM), and transmission electron microscopy (TEM). Both TEM and SEM images show that $MnO_2$ nanoplatelets are homogeneously distributed on the graphene nanosheets. The electrochemical properties were tested by cyclic voltammetry, galvanostatic charge–discharge experiments. The nanocomposite exhibited high lithium capacity (905 mAh $g^{-1}$ at 100 mA $g^{-1}$). The superior lithium storage capability can be attributed to the "open" structure: the large effective surface area and short diffusion paths.

**Keywords** $MnO_2$ · Graphene nanosheets · Lithium ion batteries

## 1 Introduction

Lithium ion batteries (LIBs) are playing an increasingly significant role in the market of energy storage and conversion devices due to the high energy density, long cycle life, low self-discharge, high operating voltage, wide temperature window and no ″memory effect″ [1, 2]. Graphite has been employed as a practical electrode with the theoretical gravimetric capacity of 372 mAh $g^{-1}$. However, considerable efforts have been made to explore high-performance electrode materials for high-power LIBs [3]. Manganese dioxide is considered as a good candidate because of its high theoretical capacity (1,232 mAh $g^{-1}$) [4]. Unfortunately, the practical application of $MnO_2$ is hampered by its poor electrical conductivity and large volume expansion during lithium intercalation/de-intercalation process [5]. According to previous reports, hybridizing $MnO_2$ with carbon has been demonstrated to be an effective method to accommodate the strain of volume change [5–7].

Recently, graphene nanosheets (GNS), as a new kind of carbon materials, have captured much attention due to its excellent electronic conductivity, mechanical properties and high surface area [8–10]. Xing et al. [6] prepared α-$MnO_2$/graphene by a facile wet-chemical route. It was found that the growth of α-$MnO_2$ nanosheets on the surface of graphene was effective to improve the reversible capacity. Yu et al. [4] fabricated a thin film of graphene/$MnO_2$ (GWMN) nanotubes by an ultrafiltration technique. They found that the thin films present excellent rate capabilities. However, there are few reports on the uniform distribution of porous $MnO_2$ nanoplatelets on the surface of graphene for LIBs. It could be a good design if porous $MnO_2$ were sandwiched between the graphene. In this way, the nanopores could be used as buffered space for the volume change during $Li^+$ intercalation/de-intercalation. In addition, graphene offer high surface area and short diffusion pathways for the rapid transport of both electrons and $Li^+$. The structure design will result in superior cyclic performance and high reversible capacity in comparison with the ordinary $MnO_2$.

Herein, we have prepared the nanocomposite of GWMN with a porous "open" structure by one-step chemistry route. The investigation is focused on the structure and the lithium storage capacity of GWMN.

X. Li (✉) · H. Song · H. Wang · Y. Zhang · K. Du · H. Li · J. Huang
School of Materials Science and Engineering, Chongqing University, Chongqing 400045, People's Republic of China
e-mail: lixinlu@cqu.edu.cn

## 2 Experimental

### 2.1 Material preparation

All reagents were of analytical grade. The nanocomposite of GWMN nanoplatelets was synthesized via one-step chemistry route. First of all, graphite oxide (GO) was synthesized using natural graphite (30 μm) by a modified Hummers method [11]. GNS was prepared by the exfoliation of GO by microwave irradiation as described elsewhere [12]. Then, 0.1 g GNS were dissolved in 100 ml distilled water under continuous stirring. 0.2 g $MnSO_4{\cdot}H_2O$ and 0.5 mg $KMnO_4$ was added into the above solution, followed by stirring for 2 h at room temperature. The obtained products were collected by centrifuging the mixture, and then washed with distilled water and absolute ethanol several times and dried at 80 °C for 12 h. For comparison, $MnO_2$ particles were prepared by the above process without the addition of GNS.

### 2.2 Material characterization

X-ray diffraction (XRD) patterns were recorded from DMAX-2500PC using Cu/K$\alpha$ radiation ($\lambda = 1.5406$ Å). The morphology and structure of the samples were observed by field emission scanning electron microscope (FESEM, NOVA 400) and high-resolution transmission electron microscope (HRTEM, LIBRA 200FE). Specific surface area and porosity structure were measured by nitrogen adsorption/de-adsorption using an automatic adsorption system (ASAP 2020 M + C). Thermogravimetric analysis (TGA) data were collected on a thermal analysis instrument (NETZSCH STA 449C) with a heating rate of 10 °C/min in an air flow of 50 mL/min.

### 2.3 Electrochemical measurement

The working anode was prepared by mixing the samples, polyvinylidene fluoride binder and carbon black in the weight ratio 80:10:10 in *N*-methyl-2-pyrrolidone solvent. The charge–discharge characteristics were examined in CR2430 coin cells, which were assembled in an argon-filled glove box. These cells were composed of a lithium foil as the corresponding electrode, 1 M $LiPF_6$ in the volume ratio 1:1 ethyl carbon (EC)/diethyl carbonate (DEC) as the electrolyte, microporous polyethylene separator (Celgard 2500) and the prepared anode.

The cells were galvanostatically charged–discharged in the voltage range 0–3.0 V versus $Li/Li^+$ at the current densities of 50, 100 and 500 mA $g^{-1}$ via a Battery Testing System (Ningbo baite testing equipment Co., China). Cyclic voltammetry (CV) curves were collected at 0.2 mV $s^{-1}$ within the range of 0–3.0 V and electrochemical impedance spectroscopy (EIS) was performed from 1 Hz to 100 kHz frequency range using Solartron (1287+1260 8w).

## 3 Results and discussion

Figure 1 shows the SEM images of $MnO_2$, GNS, and GWMN, respectively. Figure 1a illustrates that the $MnO_2$ particles appear to be aggregates. In Fig. 1b, GNS are curled and entangled together with a layered structure. As shown in Fig. 1c, GNS presented a rough and lusterless appearance, showing that $MnO_2$ nanoplatelets are densely oriented on the surface of GNS. Magnified SEM image (Fig. 1d) shows the rough surface of the intertwined $MnO_2$ nanoplatelets, which are oriented on GNS, resulting in the "opened" structure of GWMN.

The TEM images of GNS and GWMN are shown in Fig. 2. There are corrugations and scrollings on the graphene sheets (Fig. 2a). As for GWMN (Fig. 2b), intertwined $MnO_2$ nanoplatelets tend to agglomerate to form porous particles on the surface of GNS, which agree well with the "opened" structure observed by the SEM image (Fig. 1d).

XRD patterns of the GNS, $MnO_2$, and GWMN are presented in Fig. 3. In the case of GNS, the diffraction peaks at $2\theta = 24.5°$ and 42.8° correspond to the (0 0 2) and (1 0 0), respectively. For the pure $MnO_2$ powders, the diffraction peaks at 37.3°, 66.6° can be well-assigned to the (2 1 1) and (1 1 2) planes of $\alpha$-$MnO_2$ crystal according to the standard data file (JCPDS file no. 44-0141). But the diffraction peaks for $MnO_2$ are weak and broad, indicating the amorphous crystal of the as-prepared products. GWMN show an XRD pattern (Fig. 3c) similar to that of $MnO_2$ but the (1 0 0) reflection peak of GNS has disappeared, suggesting the crystal structure of $MnO_2$ is not affected [13].

Figure 4 shows the TGA curve of $MnO_2$/GNS. The 19.4 % weight loss below 270 °C is associated with the removal of surface-adsorbed water, and the 2.5 % weight loss in the 270–510 °C temperature range is ascribed to the evaporation of adsorbed water in the lattice and the residual oxygen-containing groups on the GNS. And, the 3.4 % weight loss in the 510–600 °C temperature range should be attributed to the removal of carbon sketch by burning of graphene, and thus, the mass percentage of $MnO_2$ in the nanocomposite is 96.6 % while that of graphene is 3.4 %. Therefore, it can be deduced that the $MnO_2$ mostly contributes to the whole capacity of the $MnO_2$/GNS electrode.

Figure 5a shows the nitrogen adsorption–desorption isotherms. The increase in absorbed quantity indicates the remarkable enhancement of specific surface area when GNS are introduced to wrap the $MnO_2$ nanoplatelets. The BET specific surface area of $MnO_2$ was 49.4 $m^2$ $g^{-1}$ and the average pore volume was 0.11 $cm^3$ $g^{-1}$. With the GNS hybriding, the corresponding data of GWMN changed to be 196.4 $m^2$ $g^{-1}$ and 0.42 $cm^3$ $g^{-1}$, respectively. Figure 5b illustrates that the mesopores less than 50 nm in diameter increases greatly in the case of GWMN, leading to the striking increase in pore volume. The results clearly imply

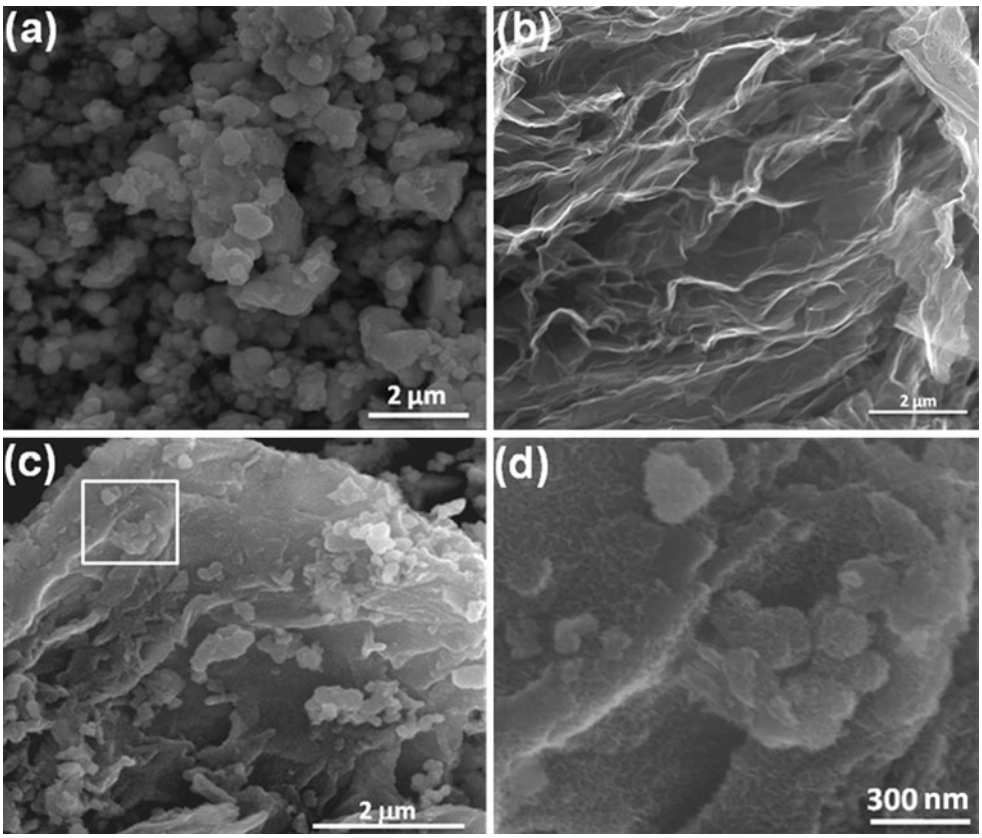


**Fig. 1** SEM images of **a** $MnO_2$, **b** GNS, **c** GWMN, **d** the enlarged image of the *rectangle* in (**c**)

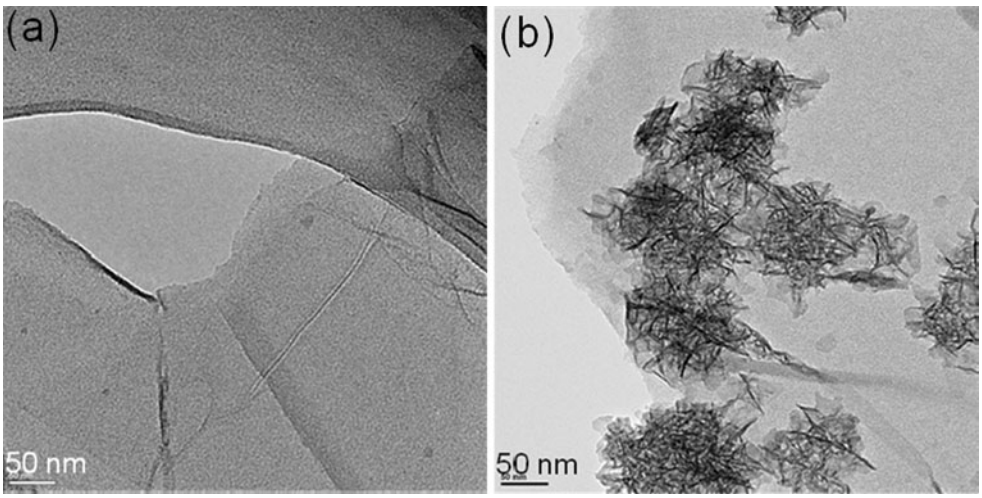


**Fig. 2** TEM images of **a** GNS, **b** GWMN

the enhancement in the surface area of GWMN, and serve as a strong evidence for the porosity of GWMN.

The electrochemical reactivity of $MnO_2$ and GWMN was initially characterized by CV. In Fig. 6a, in the first negative scan process, a cathodic peak appeared at 0.1 V, corresponding to the complete reduction of $Mn^{4+}$ to $Mn^0$ and the formation of a solid electrolyte interphase (SEI) layer [14]. From the second cycle, the peaks turn to 0.3 V, suggesting an irreversible structural or textural modifications due to the formation of $Li_2O$ and metallic manganese [15]. In the anodic process, there is a peak close to 1.3 V and a weak peak at 2.1 V, corresponding to the oxidation

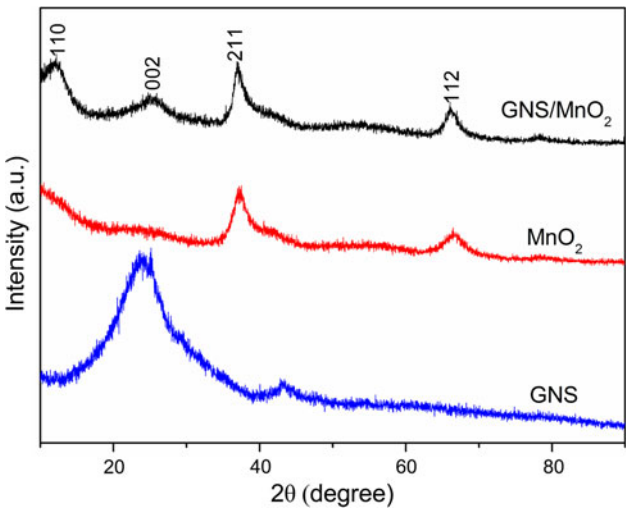


**Fig. 3** XRD patterns of **a** GNS, **b** $MnO_2$, **c** GWMN

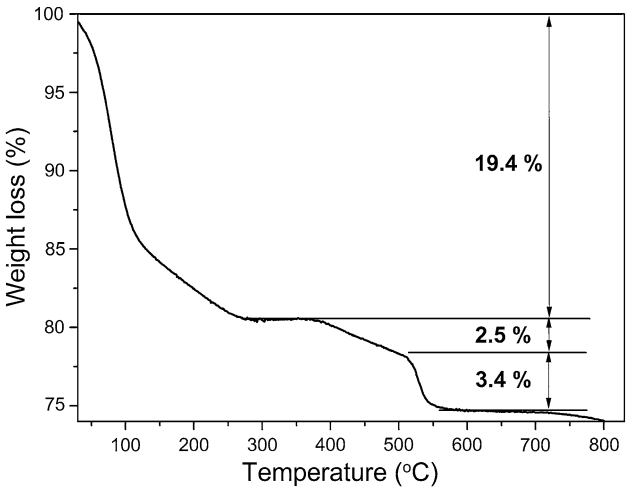


**Fig. 4** TGA curve of GWMN

of $Mn^0$ to $Mn^{4+}$ by two steps. The CV curves can be overlapped well after the second cycle. In the case of $MnO_2$ in Fig. 6b, the peak intensity and integral area of the CV curves decrease obviously with the increase of cycles, implying the poor electrochemical performance.

In agreement with the above CV analysis, two distinct voltage plateaus can be observed for $MnO_2$ and GWMN during the charge–discharge process (Fig. 6c). In comparison, there is no distinguishable plateau for GNS [16]. The discharge curve can be divided into three stages, which is similar to that of the $TiO_2$ [17]. The first stage is marked by a sharp decrease in voltage from the open-circuit potential to $\sim$0.3 V, which is associated with very small amount of Li ions insertion. The second stage is caused by the process of lithium insertion into $MnO_2$, corresponding to the plateau region at $\sim$0.3 V. The third stage exhibits a long gradual decay of the voltage after the plateau region, proving the insertion of lithium into the surface structure of the material. In addition, the initial discharge specific capacity of GWMN is about 1,421 mAh $g^{-1}$, which is higher than that of the $MnO_2$ (931 mAh $g^{-1}$) and the GNS (1,329 mAh $g^{-1}$). The initial charge capacities are 416, 1009, and 905 mAh $g^{-1}$ for $MnO_2$, GNS, and GWMN, respectively. The capacity loss may result from the incomplete conversion reactions and irreversible lithium loss due to the formation of a SEI layer [5, 15]. It can be seen that the GWMN electrode exhibits an irreversible capacity loss of 36 % in comparison with 55 % for $MnO_2$, indicating that the "open" structure provides fast electron transport through the electrode. Besides, GWMN exhibits much better rate capability compared to the $MnO_2$ and GNS electrodes at the different rates of 50, 100, and 500 mA $g^{-1}$ (Fig. 6d). Notably, a reversible capacity of 341 mAh $g^{-1}$ can be obtained at the highest current rate of 500 mA $g^{-1}$, further proving the efficient $Li^+$ intercalation/de-intercalation. More importantly, a stable capacity of 630 mAh $g^{-1}$ can be resumed when the current rate is returned to 50 mA $g^{-1}$.

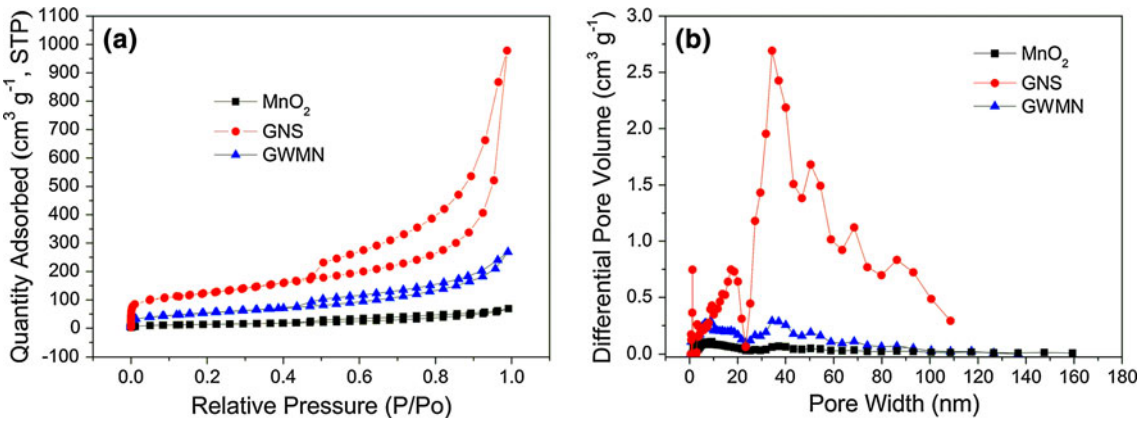


**Fig. 5** Nitrogen adsorption/de-adsorption curves of $MnO_2$, GNS and GWMN

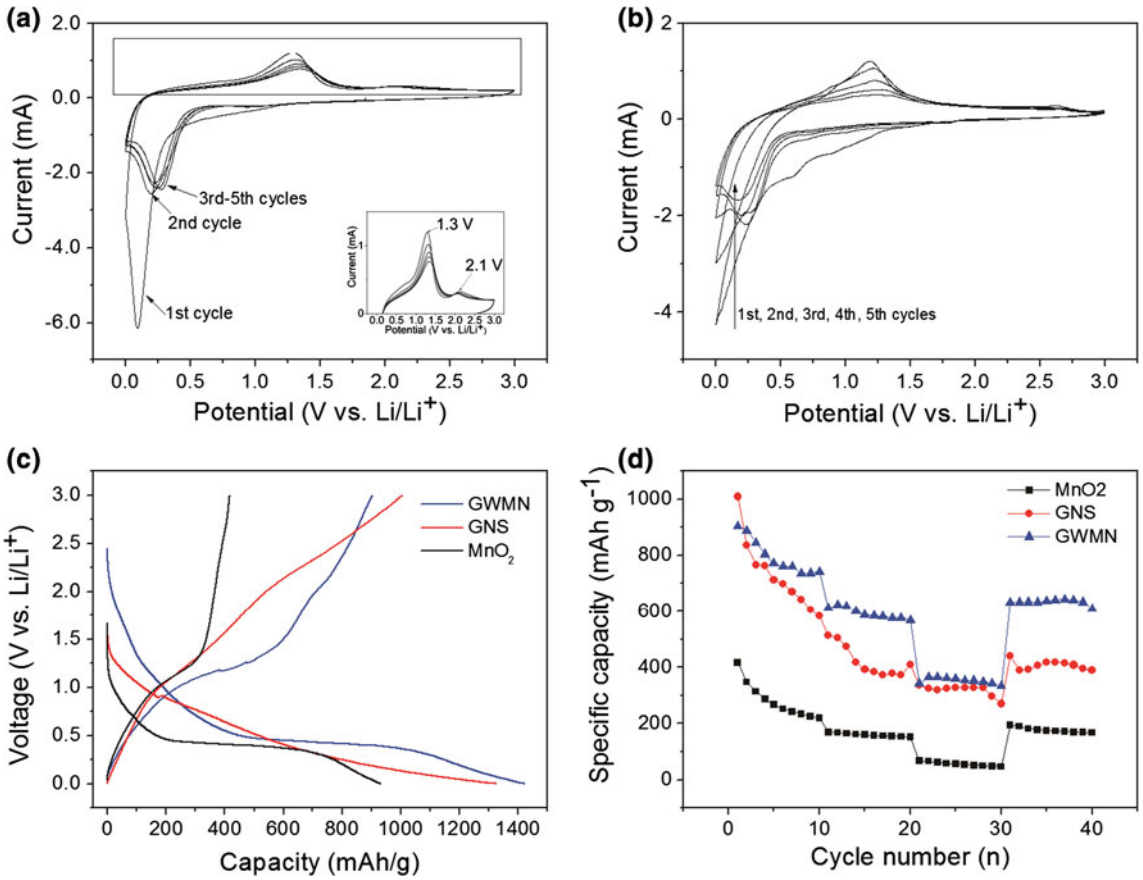


**Fig. 6** **a** Cyclic voltammetry profile of GWMN at a scanning rate of 0.2 mV $s^{-1}$, the *inset* shows the enlarged image of the *rectangle* in (**a**), **b** cyclic voltammetry profile of $MnO_2$ at a scanning rate of 0.2 mV $s^{-1}$, **c** the initial charge–discharge curves of $MnO_2$, GNS, and GWMN at current density of 50 mA $g^{-1}$, **d** rate capability of $MnO_2$, GNS, and GWMN at different current densities

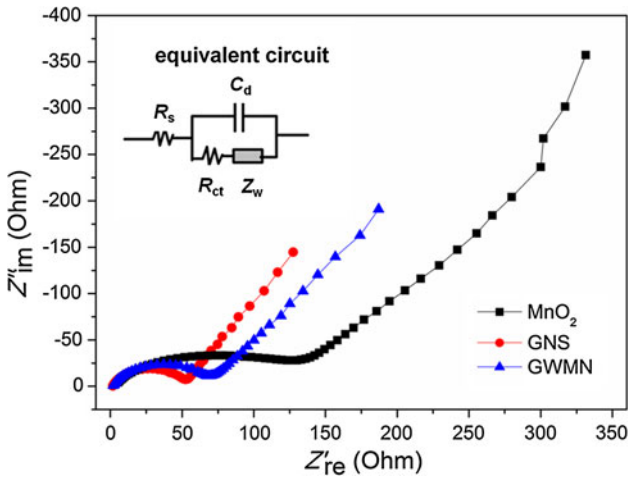


**Fig. 7** EIS spectra of GNS, $MnO_2$ and GWMN electrode in 1 M $LiPF_6$/EMC–DMC (1:1 in v $v^{-1}$) in the frequency range from 1 Hz to 100 kHz

Figure 7 presents the Nyquist plots of pure GNS, $MnO_2$, and GWMN electrodes. All the EIS spectra are combinations of a semicircle in high frequencies and a straight line in low frequencies. The equivalent circuit for the Nyquist plots is shown as an inset in Fig. 6. In this equivalent circuit, the symbols $R_s$, $R_{ct}$, $C_d$, and $Z_w$ denote the solution resistance, charge-transfer resistance, capacitance of the double layer, and Warburg impedance, respectively [18]. The intercepts with real impedance [Re($Z$)] axis of pure GNS, $MnO_2$, and GWMN electrodes, which is considered to be the total electronic resistance of the electrode materials [19], is calculated to be 53, 133 and 69 Ω, respectively. Compared with the $MnO_2$ electrode, the decrease in the semicircles for the GWMN electrode can be ascribed to the increase in the effective electrochemical interface by improved electron supply.

The work revealed that GWMN showed high reversible capacity and rate stability as an anode material for LIBs. Li et al. [20] reported that Li extraction reaction could occur where the carriers can be sufficiently transported through the metal oxide phase. Thus, Li ion transport could be enhanced by the "open" structure, which facilitates the penetration of solvated lithium ion. And, graphene, the conductive backbone, could enhance the lithium capacities of pure $MnO_2$ materials through improving their electrical

conductivity [21]. As a consequence, the synergistic effect of the "open" structure and conductive, flexible GNS makes a perspective candidate for LIBs.

## 4 Conclusions

In summary, a nanocomposite of GWMN nanoplatelets with "open" structure has been successfully synthesized by a simple chemistry route. The porous $MnO_2$ is composed of interconnected $MnO_2$ nanoplatelets. The unique structure enables to transport both electrolyte ions and electrons rapidly throughout the whole composite, facilitating the electrochemical reaction activity of $MnO_2$ agglomerates. As a result, the nanocomposite exhibited an enhanced charge capacity of 905 mAh $g^{-1}$ at 50 mA $g^{-1}$ compared to that of pure $MnO_2$ (416 mAh $g^{-1}$). With the improved rate capabilities, the nanocomposite demonstrated as one of the promising anode materials for LIBs.

**Acknowledgments** The authors would like to thank the financial support from the Fundamental Research Funds for the Central Universities of China (Nos. CDJZR10 13 88 01 and CDJXS10 13 11 58) and National Natural Science Foundation of China (No. 51172293).

## References

1. Winter M, Besenhard JO, Spahr ME, Novák P (1998) Insertion electrode materials for rechargeable lithium batteries. Adv Mater 10:725–763
2. Goodenough JB (2012) Rechargeable batteries: challenges old and new. J Solid State Electrochem 16:2019–2029
3. Wu Z, Ren W, Wen L, Gao L, Zhao J, Chen Z, Zhou G, Li F, Cheng H (2010) Graphene anchored with Co3O4 nanoparticles as anode of lithium ion batteries with enhanced reversible capacity and cyclic performance. ACS Nano 4:3187–3194
4. Yu A, Park HW, Davies A, Higgins DC, Chen Z, Xiao X (2011) Free-standing layer-by-layer hybrid thin film of graphene–$MnO_2$ nanotube as anode for lithium ion batteries. J Phys Chem Lett 2:1855–1860
5. Reddy ALM, Shaijumon MM, Gowda SR, Ajayan PM (2009) Coaxial $MnO_2$/carbon nanotube array electrodes for high-performance lithium batteries. Nano Lett 9:1002–1006
6. Xing L, Cui C, Ma C, Xue X (2011) Facile synthesis of $\alpha$-$MnO_2$/graphene nanocomposites and their high performance as lithium-ion battery anode. Mater Lett 65:2104–2106
7. Xia H, Lai M, Lu L (2010) Nanoflaky $MnO_2$/carbon nanotube nanocomposites as anode materials for lithium-ion batteries. J Mater Chem 20:6896–6902
8. Geim AK (2009) Graphene: status and prospects. Science 324:1530–1534
9. Novoselov KS, Geim AK, Morozov SV, Jiang D, Zhang Y, Dubonos SV, Grigorieva IV, Firsov AA (2004) Electric field effect in atomically thin carbon films. Science 306:666–669
10. Stankovich S, Dikin DA, Dommett GHB, Kohlhaas KM, Zimney EJ, Stach EA, Piner RD, Nguyen ST, Ruoff RS (2006) Graphene-based composite materials. Nature 442:282–286
11. Marcano DC, Kosynkin DV, Berlin JM, Sinitskii A, Sun ZZ, Slesarev A, Alemany LB, Lu W, Tour JM (2010) Improved synthesis of graphene oxide. ACS Nano 4:4806–4814
12. Li X, Song H, Wang H, Li H, Zhang Y, Huang J (2012) A comparison of exfoliation methods on microstructure and electrochemical performance of graphene nanosheets for supercapacitors. J New Mater Electrochem Syst 15:97–101
13. Zhu J, He J (2012) Facile synthesis of graphene-wrapped honeycomb $MnO_2$ nanospheres and their application in supercapacitors. ACS Appl Mater Interfaces 4:1770–1776
14. Sun B, Chen Z, Kim H, Ahn H, Wang G (2011) MnO/C core–shell nanorods as high capacity anode materials for lithium-ion batteries. J Power Sources 196:3346–3349
15. Wu M, Chiang PJ, Lee J, Lin J (2005) Synthesis of manganese oxide electrodes with interconnected nanowire structure as an anode material for rechargeable lithium ion batteries. J Phys Chem B 109:23279–23284
16. Yoo E, Kim J, Hosono E, Zhou H, Kudo T, Honma I (2008) Large reversible Li storage of graphene nanosheet families for use in rechargeable lithium ion batteries. Nano Lett 8:2277–2282
17. Chen JS, Tan YL, Li CM, Cheah YL, Luan D, Madhavi S, Boey FYC, Archer LA, Lou XW (2010) Constructing hierarchical spheres from large ultrathin anatase $TiO_2$ Nanosheets with nearly 100 % exposed (001) facets for fast reversible lithium storage. J Am Chem Soc 132:6124–6130
18. Li XL, Du K, Wang H, Song HF, Liu HD, Li HY, Zhang YX, Huang JM (2011) Electrochemical performance of network nanocomposite of spherical graphite with various carbon conductors. Int J Electrochem Sci 6:4411–4421
19. Lee CY, Tsai HM, Chuang HJ, Li SY, Lin P, Tseng TY (2005) Characteristics and electrochemical performance of supercapacitors with manganese oxide-carbon nanotube nanocomposite electrodes. J Electrochem Soc 152:A716–A720
20. Li H, Balaya P, Maier J (2004) Li-storage via heterogeneous reaction in selected binary metal fluorides and oxides. J Electrochem Soc 151:A1878–A1885
21. Wang H, Cui L, Yang Y, Sanchez Casalongue H, Robinson JT, Liang Y, Cui Y, Dai H (2010) $Mn_3O_4$−graphene hybrid as a high-capacity anode material for lithium ion batteries. J Am Chem Soc 132:13978–13980